Interlaminar stress analysis for carbon/epoxy composite space rotors

Chong Ee Lian[1], Renuganth Varatharajoo[1,*], Nurulasikin Mohd Suhadis[2]

[1]Department of Aerospace Engineering,
University Putra Malaysia, 43400 Selangor, Malaysia.
*E-mail: renu99@gmx.de
[2]School of Aerospace Engineering,
Universiti Sains Malaysia, 14300 Penang, Malaysia.

ABSTRACT

This paper extends the previous works that appears in the International Journal of Multiphysics, Varatharajoo, Salit and Goh (2010). An approach incorporating cohesive zone modelling technique is incorporated into an optimized flywheel to properly simulate the stresses at the layer interfaces. Investigation on several fiber stacking sequences are also conducted to demonstrate the effect of fiber orientations on the overall rotor stress as well as the interface stress behaviour. The results demonstrated that the rotor interlaminar stresses are within the rotor materials' ultimate strength and that the fiber direction with a combination of 45°/-45°/0° offers the best triple layer rotor among the few combinations selected for this analysis. It was shown that the present approach can facilitate also further investigation on the interface stress behaviour of rotating rotors.

1. INTRODUCTION

The flywheel energy storage technology is indeed a promising technology in replacing the conventional battery as energy storage devices for spacecraft. The simultaneous use of the flywheels as attitude control actuators enables the further reduction in spacecraft operating mass. In the context of flywheels in space applications, it is observed that the operation of the flywheel has been well investigated in the works of Varatharajoo and Kahle (2005) on the feasibility of the combined energy and attitude control system (CEACS); Varatharajoo and Fasoulas (2002, 2005), Varatharajoo (2006), Roithmayer et al. (2003), as well as Tsiotras et al. (2001) on the CEACS attitude control performances; Varatharajoo, Wooi and Mailah (2011) where Active Force Control (AFC) techniques has been integrated for the enhancement of the attitude control of CEACS; and Varatharajoo (2004) on CEACS for small satellites. Other works on CEACS can be found in Varatharajoo and Filipski Abdullah (2004); Varatharajoo and Ahmad (2004); Varatharajoo, Ibrahim, Harun, Filipski Abdullah (2005). But, none of the works have investigation done on the flywheel operating speed. In view of this circumstance, the critical operating speed for the energy storage application has been investigated by Varatharajoo, Salit and Goh (2010); however, the interlaminar problems remained unaddressed in the mentioned work.

With the increasing use of laminated composites in the flywheel rims where weight savings is of paramount concern, thus rising the need in developing an appropriate models to predict the stress behavior of these composites as the interfacial surfaces of a laminate are planes of minimum strength (Pagano, N.J. & Pipes, R. B., 1973) due to discontinuities in the load path, such as free edges and notches (Wilkins, 1983). Furthermore, the shell curvature effect of the rings has also been attributed to the presence of high interlaminar

stresses (Edward, K.T., Wilson, R.S. and McLean, S.K., 1989; Lagace, P.A., 1983). In addition, with a different material for each ring of the multi rings, the interlaminar stresses might also be induced due to the sudden transition of material properties or material discontinuity (Tahani, 2005). Yet till date, the interlaminar behaviour has only been investigated for the two layer rotating rotor in the analysis performed by Tahani (2005); instead, this work presents extends the double layer interlaminar stress problem to the triple layer interlaminar stress analysis. In addition, ply orientations also play an important role in altering the stress distribution of composite laminates. In bonded repair of cracks in aircraft components, laminated composite patch with ply orientations of 0¡, +45¡, -45¡ and 90¡ have been favourable with the +45¡, -45¡ and 90¡ orientation to crack direction being identified as the optimal design where variable flight loadings are concern (Chue and Liu, 1995; Baker and Jones, 1988). Thus, it is also of importance that the fiber recipe be considered in the design of such structures, especially for flywheels spun at high operating speed.

Finite element analysis using ANSYS^{TM} is employed for three high speed rotor configurations; i.e., single layer, double layer and triple layer rotor after considering the relevant properties involved, e.g., composite materials, rotor dimensions and rotor speed. The single layer rotor of IM6 carbon epoxy composite has been built via numerical modelling with finite element analysis (FEA) and the results has been compared with the analytical solution for the validation of the model. The validated model is then extended to the double layer model where the novel approach of using the cohesive zone modelling technique to simulate the interface stress behaviour has been incorporated to the double layer model which is compared with the analytical and numerical solution by Tahani. It is discovered that the results for the cohesive zone model closely approximate the trends of the analytical solutions by Tahani (2004), indicating the cohesive zone modeling approach as a feasible conceptual design tool for future replication in simulating stresses at the interface of material discontinuity. The validated model also forms the fundamental tool in the highlight of this paper on the investigation of the interlaminar stresses of the triple layer rotor. The numerical solutions are discussed from the stress distribution point of view. Finally, several variation of the fiber orientation combination has been performed on the triple layer rotor. The work demonstrates how fiber orientation alters the stress distribution of the flywheel rotor as well as the use of cohesive zone elements in simulating the three dimensional stress effects at the interface.

2. SPACECRAFT FLYWHEEL

The stresses for the orthotropic can be represented as functions of the radius by several equations as shown by Varatharajoo, R., Salit, M.S., and Goh, K.H. (2010). The radial displacement is as follow:

$$ur = C_1 r^k + C_2 r^{-k} - \frac{\rho \omega^2 (1 - \upsilon r \theta \upsilon \theta r)}{9 E_r - E\theta} r^3 \tag{2.1}$$

Here, the radial stress, σ_r, and tangential stress, σ_θ, as functions of the radius are as described below.

$$\sigma_r = \frac{E_r(k + \upsilon_{\theta r})}{1 - \upsilon_{r\theta}\upsilon_{\theta r}} C_1 r^{k-1} + \frac{E_r(-k + \upsilon_{\theta r})}{1 - \upsilon_{r\theta}\upsilon_{\theta r}} C_2 r^{-k-1} - \frac{\rho \omega^2 (3 + \upsilon_{\theta r}) E_r}{9 E_r - E_\theta} r^2 \tag{2.2}$$

Table 2.1 Safety Factors for IM6 Carbon/ epoxy

Parameter	Longitudinal direction	Transverse direction	
Stress	Tensile	Tensile	Compressive
Maximum Strength σ_{max} [MPa]	3500	56	150
Vacuum, fatigue coefficient	0.8	0.65	
Reciprocal safety coefficient	0.9	0.9	
Over speed factor	0.9	0.9	
Total product factor f	0.65	0.53	
Usable strength $f\,\sigma_{max}$ [MPa]	2275	30	80

$$\sigma_\theta = \frac{E_\theta(1 + k\upsilon_{r\theta})}{1 - \upsilon_{r\theta}\upsilon_{\theta r}} C_1 r^{k-1} + \frac{E_\theta(1 - k\upsilon_{r\theta})}{1 - \upsilon_{r\theta}\upsilon_{\theta r}} C_2 r^{-k-1} - \frac{\rho\omega^2(1 + 3\upsilon_{r\theta})E_\theta}{9E_r - E_\theta} r^2 \tag{2.3}$$

The material constant is depicted by $k = \left(\dfrac{E_\theta}{E_r}\right)^{0.5}$; with the Poisson s ratio for the

transverse direction, $\upsilon_{r\theta} = \upsilon_{\theta r}\dfrac{E_r}{E_\theta}$; and where the equations (2.1) and (2.2) can be used to calculate the rotor stress distributions for certain operating speeds as a function of radius. The ultimate strength of the materials that are derated for space applications provides the usable material strength which has been estimated for by the rotor stress distribution. For space applications, the derated factor employed for the longitudinal tensile strength is 0.65; for transverse tensile and compressive strength, the derated factor is 0.53.

Constants C_1 and C_2 in equations (2.1) and (2.2) are to be determined after the rotor boundary conditions are set. The first boundary condition for the rotor would be σ_r being null at r = R_0 as the outer radius is a free surface where no loads are applied. Other than that, the innermost rotor functions to support of the metallic return rings belonging to that of the motor/generator magnet rings and metallic bearings (Varatharajoo & Kahle, 2005). As metals are vulnerable to high stress concentration at high speeds, segmented rings are preferred over continuous to achieve higher flywheel rotational speeds (Kirk et. al., 1997, as cited in Varatharajoo, Salit & Goh, 2010) for segmented rings introduce pressure to the inner rotor wall during high rotational operational speed, with consequent radial stresses, and as such, hoop stresses are also not allowed to exist in the material. The second boundary condition is depicted by the following equation:

$$\sigma_r(r = R_i) = -\rho_i = -\rho_{return}t_{return}R_i\omega^2 \tag{2.4}$$

Here t_{return} is the mean return ring radial thickness; and ρ_{return} is the density of return ring material (cobalt ferrite with $\rho \approx 8150 \ kg / m^3$). On the other hand, the estimates for C_2 and C_1, which are dependent on the rotational speed ω of the rotor, are as given below:

$$C_2 = \frac{1 - v_{r\theta}v_{\theta r}}{v_{\theta r} - k}\left[\rho\omega^2 \frac{3 + v_{\theta r}}{9E_r - E_\theta} R_i^k R_0^k \frac{R_i^3 R_0^k - R_i^k R_0^3}{R_0^{2k} - R_i^{2k}} + \frac{p_i}{E_r}\frac{R_0^{2k}R_i^{k+2}}{R_i^{2k} - R_0^{2k}}\right]$$ (2.5)

$$C_1 = \rho\omega^2 \frac{\left(1 - v_{r\theta}v_{\theta r}\right)\left(3 + v_{\theta r}\right)}{\left(9E_r - E_\theta\right)\left(v_{\theta r} + k\right)} R_0^{3-k} - \frac{v_{\theta r} - k}{v_{r\theta} + k} + C_2 R_0^{-2k}$$ (2.6)

In addition to the aforementioned boundary conditions, pre-stressed condition was also introduced to simulate the compressive radial stress induced by press fitting manufacturing procedures. For flywheel rotors generating high stresses in the radial and circumferential directions, the main loading is the inertia loading which, in finite element modelling environment, is applied at a fixed axis. This fixed axis rotation is independent of finite element mesh, thus allowing mesh modifications without the need to reapply the loadings for each model variation. For these models (single, double and triple layer rotor), angular velocity was applied with respect to the Z-axis the rotor at the rotor s operating limit of 50 000 rpm.

3. COHESIVE ZONE MODELING

At the interface, a cohesive zone as a separate region or surface with zero thickness can be used to properly represent the interface and its constitutive behaviour. The cohesive zone model with properties unique to both the adjacent composite materials consists of a constitutive relation between the traction vector, T, acting on the interface and the corresponding interfacial separation, δ, (displacement jump across the interface). As the cohesive surface separates due to the occurrence of damage growth, the traction initially increases, reaching a maximum value and then approaching zero as the separation continues to increase; and depending on the form of the T-δ functions, CZMs can be categorized as multilinear, polynomial, trigonometric and exponential, with the exponential cohesive zone law being the more popular of all. The exponential cohesive law has several advantages as compared to other cohesive zone laws i.e. a phenomenological description of contact is automatically achieved in normal compression; and that the tractions and their derivatives are continuous which is attractive from an implementation (i.e. it is more stable than discontinuous models such as the bilinear model) and computational point of view. However, the exponential cohesive law of Xu and Needleman only realistically describes the coupling between normal and tangential direction in a specific case of $\Phi_n = \Phi_t$. This limits the application of the cohesive zone law in mixed mode loading. Based on the model proposed by Xu and Needleman (1993, 1994), there exist an interfacial potential Φ such that

$$T = -\frac{\partial\,\Phi(\Delta)}{\partial\Delta}$$ (3.1)

Here $T = T(T_n, T_t)$ is the traction vector acting at the cohesive surface and $\Delta = \Delta(\Delta_n, \Delta_t)$ is the displacement jump vector; whereas the potential is of the form

$$\Phi\left(\Delta_n, \Delta_t\right) = \Phi_n + \Phi_n exp\left(-\frac{\Delta_n}{\delta_n}\right)\left\{\left[1 - r + \frac{\Delta_n}{\delta_n}\right]\frac{1-q}{r-1} - \left[q + \left(\frac{r-q}{r-1}\right)\frac{\Delta_n}{\delta_n}\right]exp\left(-\frac{\Delta_t^2}{\delta_t^2}\right)\right\}$$

$$q = \frac{\Phi_t}{\Phi_n} \text{ and } r = \frac{\Delta_n^{\bullet}}{\delta_n} \qquad\qquad (3.2, 3.3, 3.4)$$

In the above equations, Φ_n is the work of normal separation, Φ_t is the work of tangential separation and Δ_n^* is the value of Δ_n after complete shear separation under the condition of zero normal tension, $T_n = 0$; whereas the lengths δ_n and δ_t are the characteristic lengths of the cohesive law such that

$$T_n\left(\Delta_n\right) = \sigma_{max} \text{ at } \Delta_n = \delta_n \text{ when } \Delta_t = 0 \qquad\qquad (3.5)$$

$$T_t\left(\Delta_t\right) = \tau_{max} \text{ at } \Delta_t = \frac{\delta_t}{\sqrt{2}} \text{ when } \Delta_n = 0 \qquad\qquad (3.6)$$

Here, σ_{max} and τ_{max} are the interface normal and tangential strengths respectively. Combining the two equations given, the expressions for the normal and tangential components of traction at the interface can be obtained as below

$$T_n = \frac{\Phi_n}{\delta_n} exp\left(-\frac{\Delta_n}{\delta_n}\right)\left\{\frac{\Delta_n}{\delta_n} exp\left(-\frac{\Delta_t^2}{\delta_t^2}\right) + \frac{1-q}{r-1}\left[a - exp\left(-\frac{\Delta_t^2}{\delta_t^2}\right)\right]\left[r - \frac{\Delta_n}{\delta_n}\right]\right\} \qquad (3.7)$$

$$T_t = 2\left(\frac{\Phi_n\Delta_t}{\delta_t^2}\right)\left\{q + \left(\frac{r-q}{r-1}\right)\frac{\Delta_n}{\delta_n}\right\}exp\left(-\frac{\Delta_n}{\delta_n}\right)exp\left(-\frac{\Delta_t^2}{\delta_t^2}\right) \qquad (3.8)$$

The areas under the normal traction-separation curve and the shear traction-separation curve represent the work for normal separation (Φ_n) and shear separation (Φ_t), respectively; it is the energy required for complete separation. It can be shown using [3.5] and [3.6] that Φ_n and Φ_t take the form

$$\Phi_n = exp\left(1\right)\sigma_{max}\delta_n \text{ and } \Phi_t = \sqrt{\frac{exp\left(1\right)}{2}}\tau_{max}\delta_t \qquad\qquad (3.9)$$

The two dimensional traction separation relationship can be extended to three dimensional by tangential traction and displacement which acts perpendicular to the two previously considered directions (Gon alves et. al., 2000)

4. MODEL VALIDATION

The single layer of IM6 carbon/epoxy composite rotor model with inner radius of 0.07 m and outer radius of 0.1 m is built in ANSYS^{TM} with the operational rotating speed of 50 000 (rpm). The results obtained via numerical modelling with finite element analysis (FEA) have been compared with the analytical solution from Varatharajoo, R., Salit, M.S., and Goh, K.H., 2010.

For the double layer case, the hybrid rotating annular disks is constructed of a Kevlar/epoxy ring shrink fitted over an S-2 glass/epoxy ring (Tahani, 2005). The inner and outer radii of the disks are R_I = 0.05 m and R_O = 0.1 m and the disks is assumed to rotate with a constant angular velocity of 1000 rad/s with free- free boundary conditions. The material properties of Kevlar/epoxy in the principal material coordinate system are taken to be E_1 = 76.8 GPa, E_2 = E_3 = 5.5 GPa; G_{12} = G_{13} = 2.07 GPa, G_{23} = 1.4 GPa; and v_{12} = v_{13} = 0.34, v_{23} = 0.37, ρ =1380 kg/m^3; whereas the material properties of S-2 glass/epoxy in the principal material coordinate system are taken to be E_1 = 43.5 GPa, E_2 = E_3 = 11.5 GPa; G_{12} = G_{13} = 3.45 GPa, G_{23} = 4.12 GPa; and v_{12} = v_{13} = 0.27, v_{23} = 0.4, ρ = 2000 kg/m^3; where the subscripts 1, 2, and 3 indicate the on- axis (i.e. principal) material coordinates. For increased accuracy of the results, there are six numerical layers in each ring and thirty numerical rings in each physical ring for the hybrid rotating disk (Tahani, 2004).

For validating purposes, the model built only consists of two layers to reduce computational time. In addition, the cohesive zone modelling is also attempted on the model. The cohesive zone model selected is the exponential model by Xu and Needleman as it is readily available in the commercial finite element package ANSYS^{TM}. The normal cohesive strength used is the value of 1/10 of the elastic modulus for the epoxy which is 11.2 GPa/10 = 1.12 GPa, similar with how Xu and Needleman assumed the normal cohesive interface strength as one tenth of the elastic modulus of PMMA (Poly-Methyl-Methacrylate) in their study of numerical simulations of fast crack growth in brittle solids. (Xu & Needleman. 1994)

5.1. SINGLE LAYER ROTOR

The magnetic bearing s return rings forms the basic reference for determining of the radial thickness for the rotor analysis. A mean radial thickness of less than 3 mm is common for these return rings that are attached to the rotor; therefore, it is a requirement that the radial thickness have a mean thickness higher than this value (Varatharajoo and Kahle, 2005). The single layer rotor analytical studies can be performed with the use of Eqs. (2.1—2.6). This also acts as a reference for the numerical rotor modeling through finite element analysis (FEA). Due to the complexity of the analytical solutions for multi- layer rotors, numerical modeling through finite element analysis (FEA) is often preferred. In this context, Eqs. (2.1—2.6) also act as a reference for the numerical rotor modeling.

A numerical rotor model for a single layer carbon/epoxy rotor with an inner radius of 0.07 m and outer radius of 0.1 m (thickness of 3 mm) and height of 0.0183 m is established via finite element modeling in ANSYS^{TM} and the solutions for the rotor speed at 50 000 rpm (as shown in figure 5.1) are compared with that of the analytical solution in Figures 5.2 and 5.3 which depict the analytical stress distributions in the transverse and tangential direction respectively. The numerical modeling is in agreement with the analytical solution; therefore, the numerical model can be extended to a multi-layer rotor analysis.

(a)

POST 1

STEP = 1
SUB = 1
TIME = 1
PATH PLOT
NOD 1 = 836
NOD 2 = 588
XPLOT

(×10**4)

1384.499	
1275.638	
1166.773	
1057.908	
949.043	
840.178	
731.313	
622.448	
513.583	
404.718	
295.853	(×10**–2)

0   .6   1.2   1.8   2.4   3
    .3   .9   1.5   2.1   2.7

DIST

(b)

POST 1

STEP = 1
SUB = 1
TIME = 1
PATH PLOT
NOD 1 = 836
NOD 2 = 588
YPLOT

(×10**5)

3813.182	
3697.104	
3581.028	
3464.952	
3348.876	
3232.800	
3116.724	
3000.648	
2884.572	
2768.496	
2652.420	(×10**–2)

0   .6   1.2   1.8   2.4   3
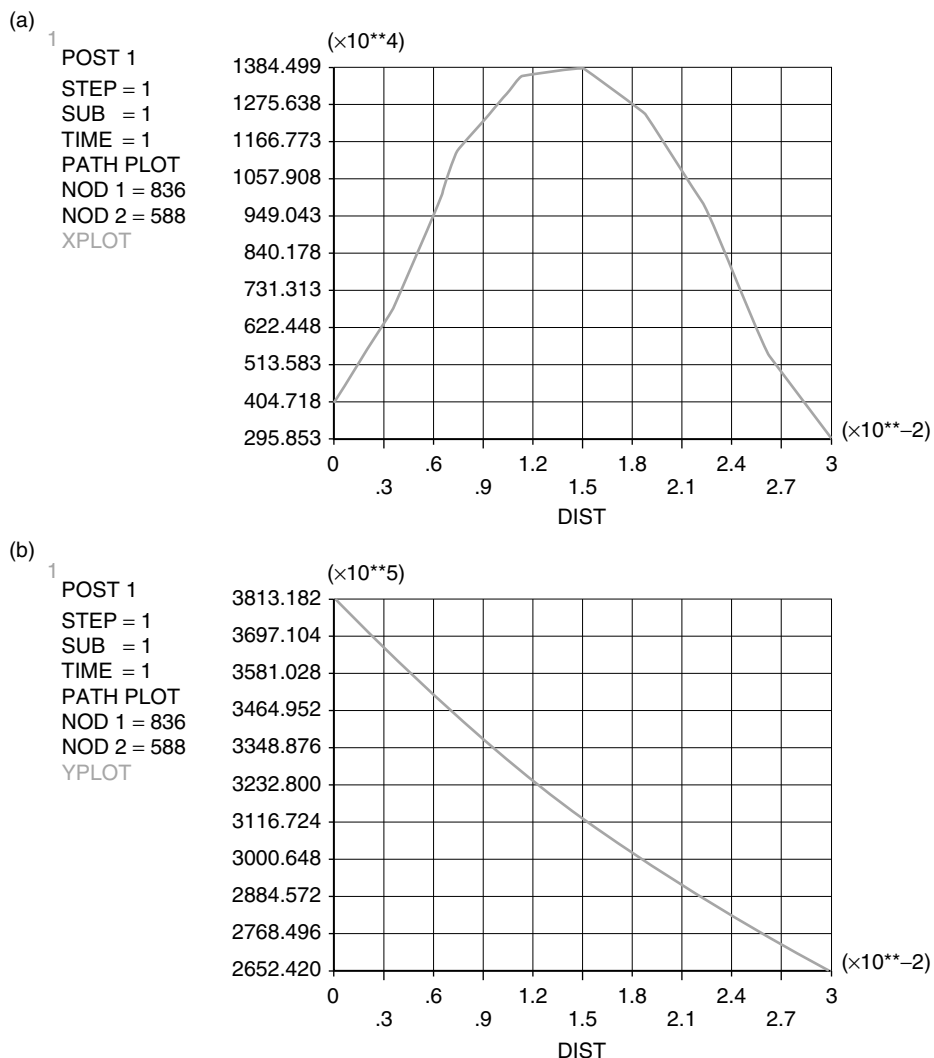   .3   .9   1.5   2.1   2.7

DIST

Figure 5.1 Distribution of stresses in (a) the transverse/ radial and (b) the longitudinal/ hoop direction for the single layer rotor for 1760 mesh elements at z = 0.4 h.

5.2. DOUBLE LAYER ROTOR

This hybrid composite disk has been originally modelled by Tahani, Nosier and Zebarjad (2005) with six numerical layers in each of the thirty numerical rings for each physical ring; and the analysis encompasses both the analytical and FEM solutions in the study to investigate the three dimensional effect of stresses at the interface. Here, a comparison between the results obtained by Tahani, Nosier and Zebarjad (2005) and that of the use of a cohesive zone as in the present flywheel rotor model was done to further verify the modelling method. For simplicity, the present cohesive zone model of 12800 mesh
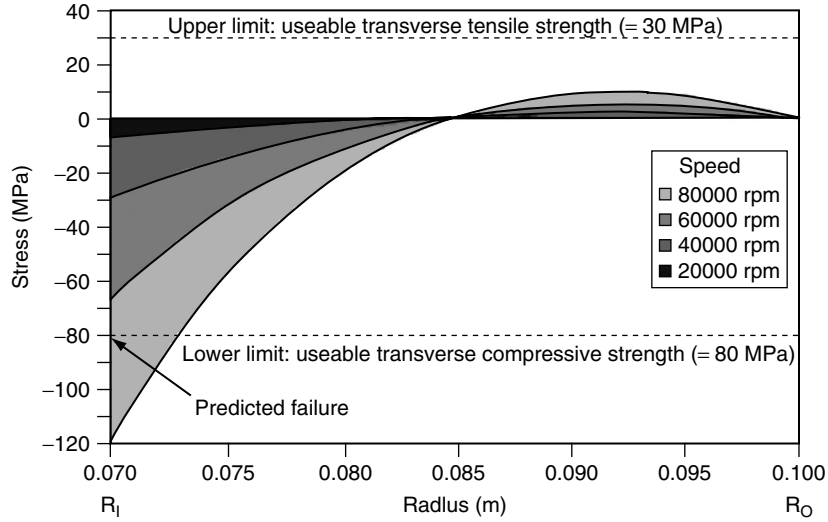
Figure 5.2   Transverse (radial) stress distributions (Varatharajoo, R., Salit, M.S., and Goh, K.H., 2010).
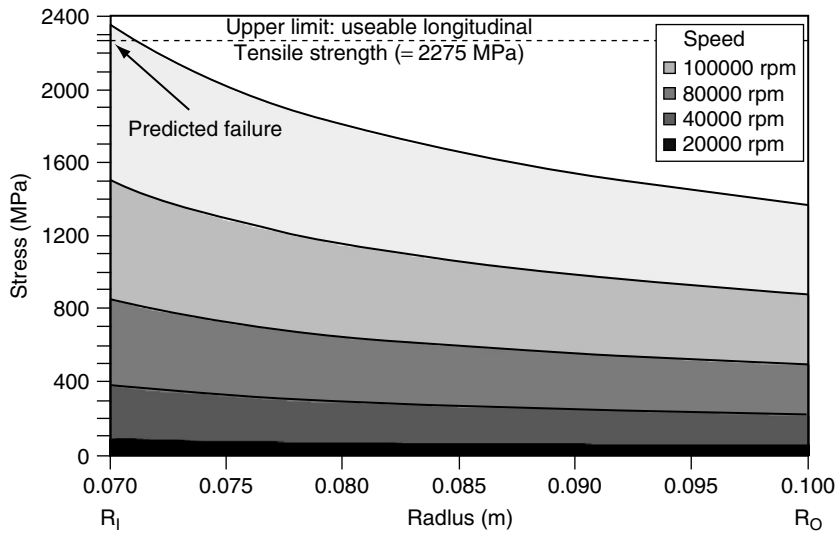

Figure 5.3   Tangential (longitudinal) stress distributions (Varatharajoo, R., Salit, M.S., and Goh, K.H., 2010).

elements only has one numerical layer for each of the two physical rings although it should be noted that the accuracy of the results increases with the number of numerical layers used.

Figure 5.4 shows the distribution of the radial stress which is non- zero and continuous at the interface, and Figure 5.5 shows the hoop stress distribution which has a marked
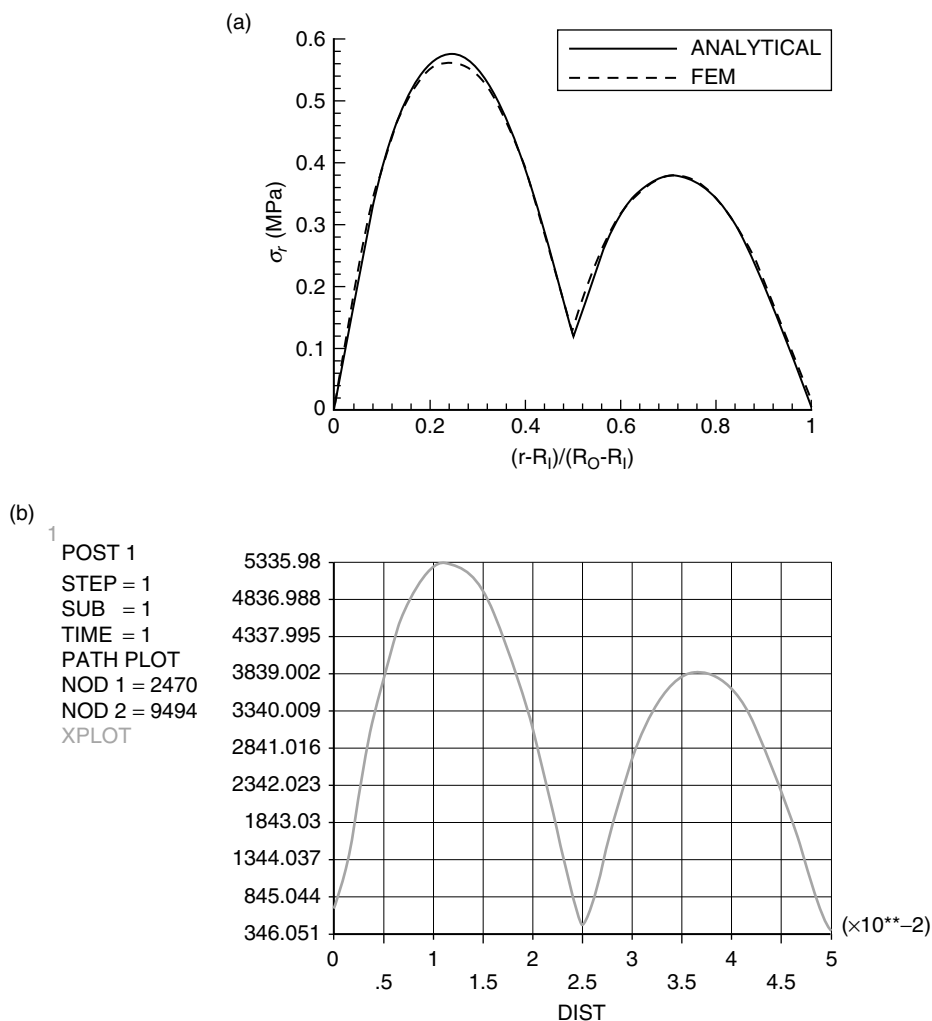
(a)

(b)

Figure 5.4 Distribution of radial stress x at Z = h/4 for the disk in free- free condition. (a) Tahani, Nosier and Zebarjad (2005). (b) numerical model with cohesive zone elements inserted.

discontinuity at the interface. Similarly, the interlaminar normal stresses σ_z is non- zero and discontinuous at the interface as shown in Figure 5.6 (b), a trend comparable to that in 5.6 (a). Figure 5.7 (a) displays the interlaminar shear stresses σ_{xz} behaviour with stresses vanishing far away from the material discontinuity. This stress pattern is similarly shown in figure 5.7 (b) where a smaller amount of numerical layers has been employed. The numerical modeling is thus in agreement with the analytical solution and hence, the validated model can be implemented in present double and triple layer problem.

The present double layer rotor model of inner radius of 0.1106 m and outer radius of 0.1174 m with MR50/LTM25 carbon/epoxy composite in the inner layer and T300/934
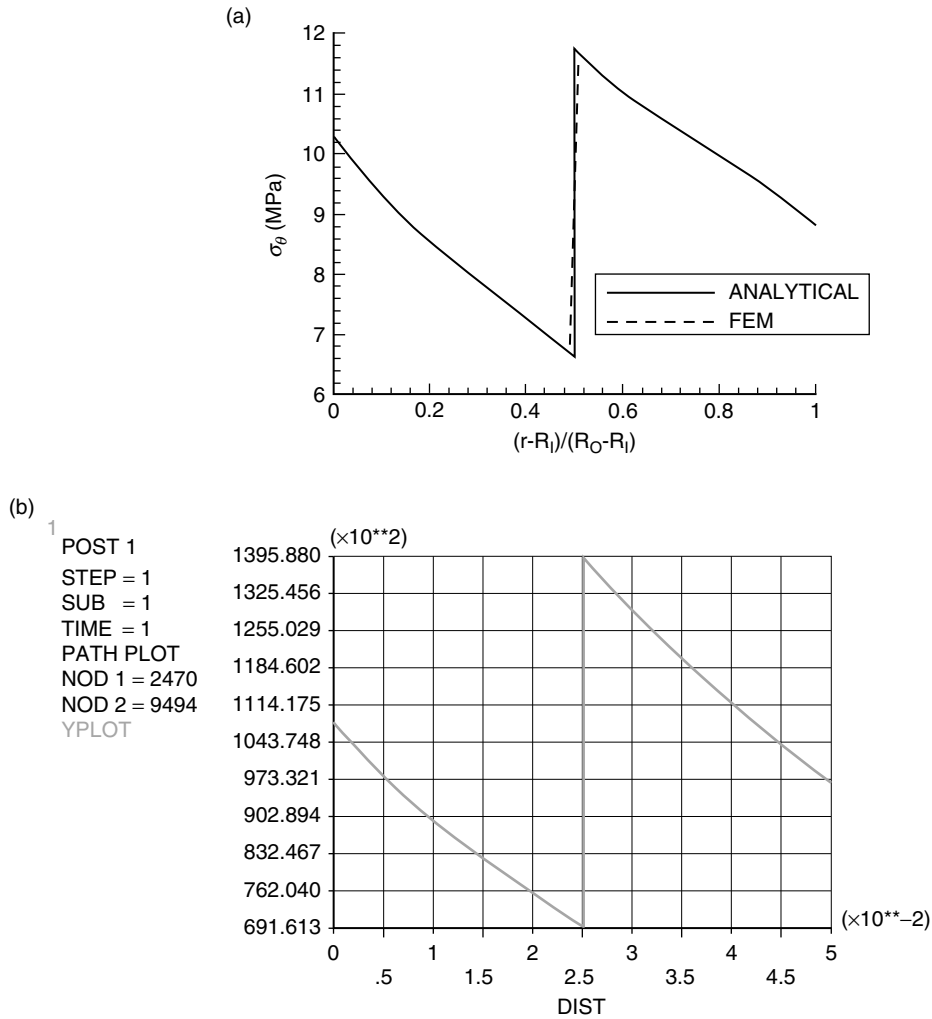
(a)

(b)

POST 1

STEP = 1
SUB = 1
TIME = 1
PATH PLOT
NOD 1 = 2470
NOD 2 = 9494
YPLOT

Figure 5.5   Distribution of hoop stress y at Z = h/4 for the disk in free- free condition. (a) Tahani, Nosier and Zebarjad (2005). (b) numerical model with cohesive zone elements inserted.

carbon/epoxy composite in the outer layer is constructed in ANSYS^{TM} and the results are presented for the rotational speed of 50,000 rpm.

Figures 5.8 (a) and (b) show the distribution of the stresses in the transverse and longitudinal direction respectively. The maximum transverse tensile stress occurs in the outer layer (6.6 MPa), which is lower than the usable transverse tensile strength of 22.79 MPa available for the outer layer; whereas the maximum transverse compressive stress occurs in the inner layer (6.4 MPa) which is still lower than the usable transverse compressive strength of 89.09 MPa available for the inner layer. About 470 MPa longitudinal tensile stress occurs in the inner layer where the usable values for the inner layer is 1313 MPa whereas the
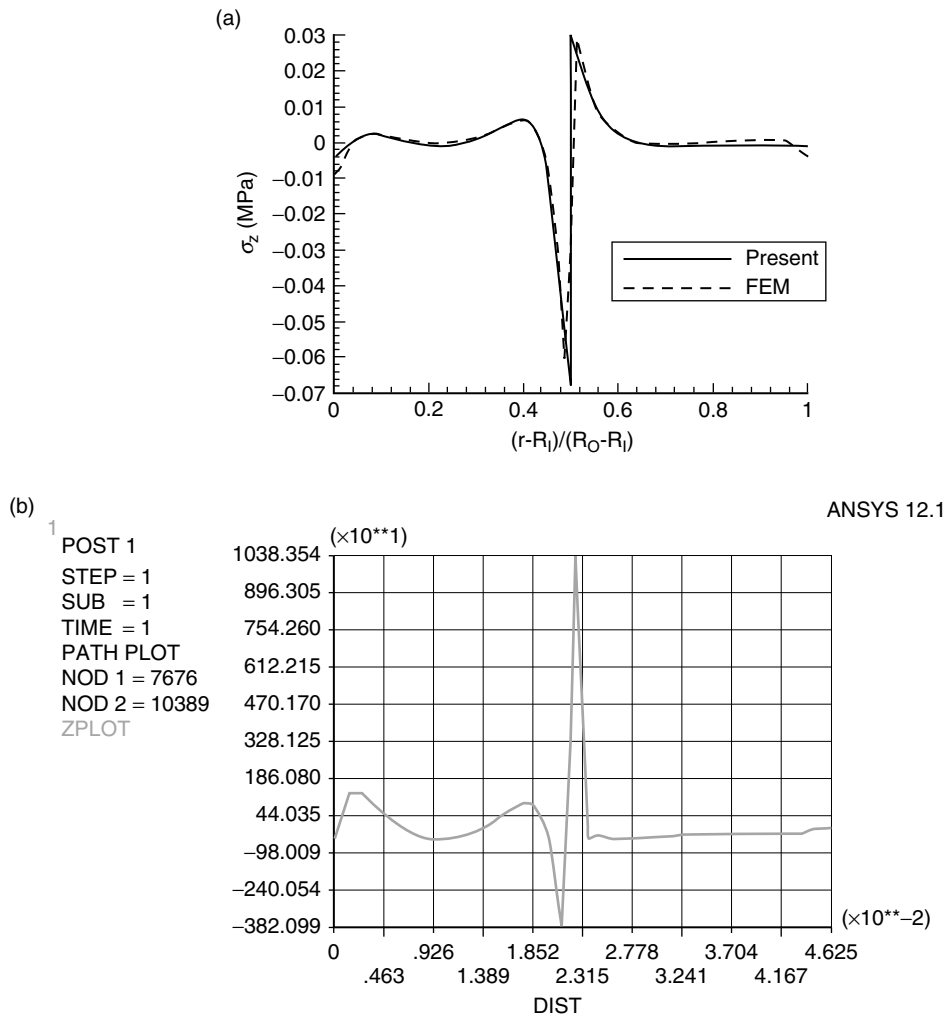
Figure 5.6   Distribution of interlaminar normal stresses σ_z at Z = h/4 for the disk in free- free condition. (a) Tahani, Nosier and Zebarjad (2005). (b) numerical model with cohesive zone elements inserted.

maximum longitudinal tensile stress occurs in the outer layer (610 MPa) layer which is below the usable longitudinal tensile stress (1313.5 MPa) in this particular layer. This longitudinal tensile stress at the outer layer is higher than that of the inner layer. As the longitudinal tensile strength is more critical at the outer layer, the triple layer rotor is presumed to be capable of improving the rotor strength. (Varatharajoo, R., Salit, M.S., and Goh, K.H., 2010).

Figure 5.8 (c) shows the interlaminar shear stresses of the rotor which ranges from -4.71 MPa for the compressive value till 4.71 MPa for the tensile value. The interlaminar normal stresses shown in figure 5.8 (d), on the other hand, has a maximum compressive value of -15.2
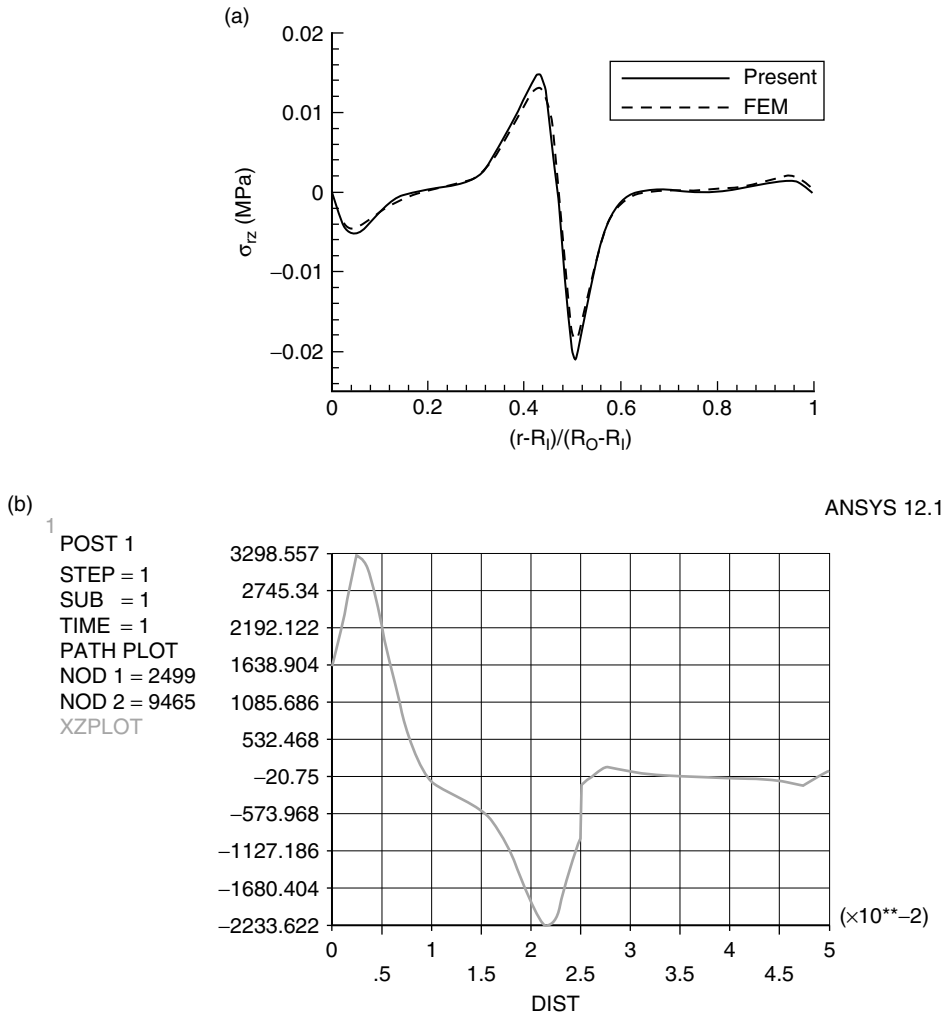
(a)

(b)   ANSYS 12.1

Figure 5.7   Distribution of interlaminar shear stresses σ_{xz} at Z = h/4 for the disk in free- free condition. (a) Tahani, Nosier and Zebarjad (2005). (b) numerical model with cohesive zone elements inserted.

MPa and a maximum tensile stress of 12.7 MPa. It is observed in Figure 4.11 that the interlaminar shear stresses σ_{xz} distribution for the double layer rotor shows a twin peak with sharp decrement at the interface for z = 0.4 h whereas at z = h location, only a single sharp peak is visible at the interface. On the other hand, the interlaminar normal stresses σ_z distributions are quite similar for both location of z = 0.4 h and z = h. The only noticeable difference is the curvier and steeper gradient of the peaks at location z = h due to the edge effects.

5.3. TRIPLE LAYER CASE
The triple layer 3D model was built via ANSYS^{TM} with thickness of 0.0183 m, inner radius of 0.1106 m and outer radius of 0.1174 m with AS4/3501-6 carbon/epoxy

(a)

POST 1
STEP = 1
SUB = 1
TIME = 1
PATH PLOT
NOD 1 = 1010
NOD 2 = 2586
XPLOT

(×10**3)

33.167
−104.968
−243.106
−381.244
−519.382
−657.520
−795.658
−933.796
−1071.934
−1210.072
−1348.210

0   1.36   2.72   4.08   5.44   6.8
    .68   2.04   3.4   4.76   6.12

(×10**−3)

DIST

(b)

POST 1
STEP = 1
SUB = 1
TIME = 1
PATH PLOT
NOD 1 = 1010
NOD 2 = 2586
YPLOT

(×10**5)

6094.942
5954.728
5814.512
5674.296
5534.080
5393.864
5253.648
5113.432
4973.216
4833.000
4692.784

0   1.36   2.72   4.08   5.44   6.8
    .68   2.04   3.4   4.76   6.12

(×10**−3)

DIST

(c)

POST 1
STEP = 1
SUB = 1
TIME = 1
PATH PLOT
NOD 1 = 1010
NOD 2 = 2586
XZPLOT

(×10**1)

2838.818
2548.724
2258.635
1968.546
1678.457
1388.368
1098.279
808.190
518.101
228.012
−62.076

0   1.36   2.72   4.08   5.44   6.8
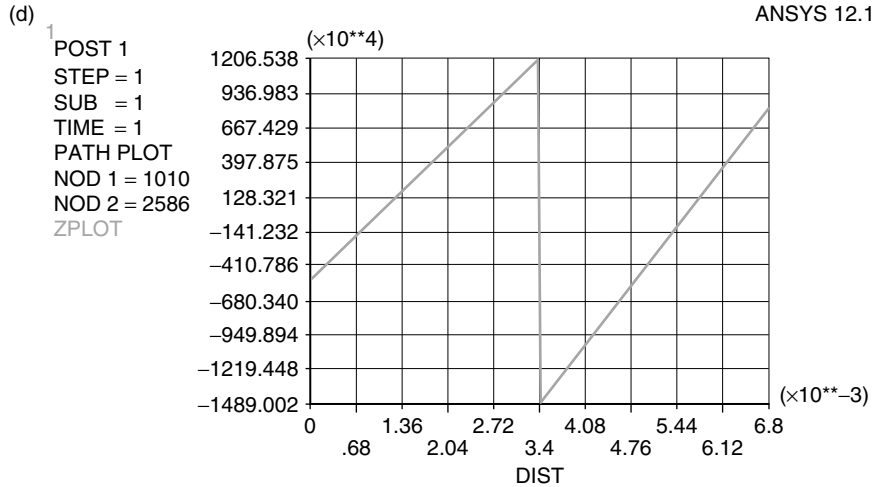   .68   2.04   3.4   4.76   6.12

(×10**−3)

DIST

Continue

Figure 5.8 Distribution of stresses for the 6400 mesh elements double layer rotor; 0°/0° stacking sequence at z = 0.4 h. (a): Stresses in the transverse/ radial direction; (b) Stresses in the longitudinal/ hoop direction; (c): interlaminar shear stresses σ_{xz}; (d): interlaminar normal stresses σ_z.

composite in the innermost layer, MR50/LTM25 carbon/epoxy composite in the middle layer and T300/934 carbon/epoxy composite in the outer layer; the double layer rotor with inner radius of 0.1106 m and outer radius of 0.1174 m with MR50/LTM25 carbon/epoxy composite in the inner layer and T300/934 carbon/epoxy composite in the outer layer; and the single layer of IM6 carbon/epoxy composite with inner radius of 0.07 m and outer radius of 0.1 m. In the study by Varatharajoo, R., Salit, M.S., and Goh, K.H. (2010), the rotor operating limit is approximately 50 000 rpm, and for that reason, the rotor is assumed to rotate with a constant angular velocity of 50 000 rpm. The material properties for the unidirectional AS4/3501-6 carbon epoxy is E_{11} = 142 GPa, E_{22} = 10.3 MPa; G_{12} = 7.2 GPa; v_{12} = 0.27 and ρ = 1580 kg/m³; for unidirectional MR50/LTM25 carbon/ epoxy is E_{11} = 155 GPa, E_{22} = 7.31 MPa; G_{12} = 4.19 GPa; v_{12} = 0.345 and ρ = 1520 kg/m³; and for T300/934 carbon/ epoxy is E_{11} = 148 GPa, E_{22} = 9.65 MPa; G_{12} = 4.55 GPa; v_{12} = 0.30 and ρ = 1500 kg/m³.

Figure 5.9 (a) displays the stress distribution in the radial direction. For the -45¡/0¡/-45¡ stacking sequence, the maximum transverse tensile stress occurs in the innermost layer (74.9 MPa) which is higher than the usable transverse tensile strength of 30.21 MPa available for the inner layer; whereas the maximum transverse compressive stress occurs in the middle layer (11.5 MPa) which is still lower than the usable transverse compressive strength of 76.85 MPa available for the middle layer. For the 45¡/-45¡/0¡ combination, the maximum transverse tensile stress occurs in the outermost layer (18.4 MPa) which is lower than the usable transverse tensile strength of 22.79 MPa available for the outer layer; whereas the maximum transverse compressive stress occurs in the outer layer (17.3 MPa) which is still lower than the usable transverse compressive strength of 89.04 MPa available for the outer layer.

(a)

POST 1
STEP = 1
SUB = 1
TIME = 1
PATH PLOT
NOD 1 = 1993
NOD 2 = 10664
XPLOT

(×10**3)

4586.331
4130.599
3674.865
3219.131
2763.397
2307.663
1851.929
1396.195
940.461
484.727
28.993

(×10**–3)

0   1.2   2.4   3.6   4.8   6
  .6   1.8   3   4.2   5.4
DIST

(b)

POST 1
STEP = 1
SUB   = 1
TIME = 1
PATH PLOT
NOD 1 = 1993
NOD 2 = 10664
XPLOT

(×10**3)

3377.443
3057.791
2738.137
2418.483
2098.829
1779.175
1459.521
1139.867
820.213
500.559
180.905

(×10**–3)

0   1.2   2.4   3.6   4.8   6
  .6   1.8   3   4.2   5.4
DIST

(c)

POST 1
STEP = 1
SUB   = 1
TIME = 1
PATH PLOT
NOD 1 = 1993
NOD 2 = 10664
XPLOT

(×10**3)

2929.456
2650.960
2372.463
2093.966
1815.469
1536.972
1258.475
979.978
701.481
422.984
144.487

(×10**–3)

0   1.2   2.4   3.6   4.8   6
  .6   1.8   3   4.2   5.4
DIST

Figure 5.9   Distribution of the radial stress σ_r at z = 0.4 h for the stacking sequence of (a) -45°/0°/-45°; (b) 45°/-45°/0° and (c) -45°/45°/-45°.

Figure 5.10 (b) shows that the maximum longitudinal tensile stress occurs in the innermost layer (783 MPa) layer -45¡/0¡/-45¡ stacking sequence which is below the usable longitudinal tensile stress (1482 MPa) in this particular layer. About 398 MPa and 610 MPa longitudinal tensile stresses occurs in the middle layer and outer layer where the usable values for these layers are 1313 MPa and 1313.35 MPa respectively. This concurred with the condition that the longitudinal tensile stress is more critical at the outer layer of the rotor. For the 45¡/-45¡/0¡ stacking sequence, the maximum longitudinal tensile stress occurs in the innermost layer (772 MPa) layer which is below the usable longitudinal tensile stress (1482 MPa) in this particular layer. About 474 MPa and 474 MPa longitudinal tensile stresses occurs in the middle layer and outer layer where the usable values for these layers are 1313 MPa and 1313.35 MPa respectively. The 45¡/-45¡/0¡ configuration has, similarly, a maximum longitudinal tensile stress in the innermost layer (737 MPa) layer which is below the usable longitudinal tensile stress (1482 MPa) in this particular layer. About 470 MPa and 546 MPa longitudinal tensile stresses occurs in the middle layer and outer layer where the usable values for these layers are 1313 MPa and 1313.35 MPa respectively.

Figures 5.11 and 5.12 exhibit the flywheel s interlaminar shear and normal stresses respectively. For the -45¡/0¡/-45¡ stacking sequence, the maximum interlaminar shear stress is 52.1 MPa in both the tensile and compressive direction whereas for the interlaminar normal stress, the value ranges from -101 MPa for compressive and 107 MPa for tensile stresses. On the other hand, the interlaminar shear stress for the fiber orientation of 45¡/-45¡/0¡ has a range from a compressive value of -13.7 MPa to 13.7 MPa in tensile as well as a maximum compressive normal stress of -56.7 MPa and a maximum tensile stress of 50 MPa; whereas the interlaminar shear stresses σ_{xz} distribution for the -45¡/45¡/-45¡ stacking sequence ranges from -17.4 MPa till 17.4 MPa, with interlaminar normal stresses σ_z in the range of between a maximum tensile stress of 43.8 MPa and a maximum compressive stress of -48.9 MPa.

With a maximum traction value of 10.7 MPa and minimum -16.3 MPa for the -45¡/0¡/-45¡ stacking sequence; 8.12 MPa and -8.85 MPa for the 45¡/-45¡/0¡ stacking sequence; and 10.7 MPa in tension, -16.3 MPa in compression for the -45¡/45¡/-45¡ stacking sequence, it is discovered that the traction values are still within the usable strength of the IM6 carbon/epoxy which are 30 MPa in the transverse tensile direction and 80 MPa in the compressive tensile direction.

In general, the transverse stresses are non-zero and discontinuous at the interface, decaying to zero at the boundaries corresponding to the free-free boundary conditions of the flywheel rotor; whereas the longitudinal stresses are generally higher than the transverse stresses, and are discontinuous at the interface. Where interlaminar stresses are concerned, severe out- of- plane stresses are noted at the interfaces where the sudden material transitions occur. The investigation of these stresses are thus, especially crucial, as the initiation of these stresses have been attributed to the onset of delamination and transverse cracking unique to hoop wound composite rotors, which if are to propagate to a substantial region of the rotor might result in the subsequent loss of strength and stiffness that would adversely affects the smooth operation of the flywheel.

Comparison between several of the fiber orientations also revealed that the rotor interlaminar stresses are within the rotor materials ultimate strength and that the 45¡/-45¡/0¡ fiber direction combination presents the best triple layer rotor based on its lower traction stress levels at the interface as well as its overall and lower tensile stresses in the radial direction.
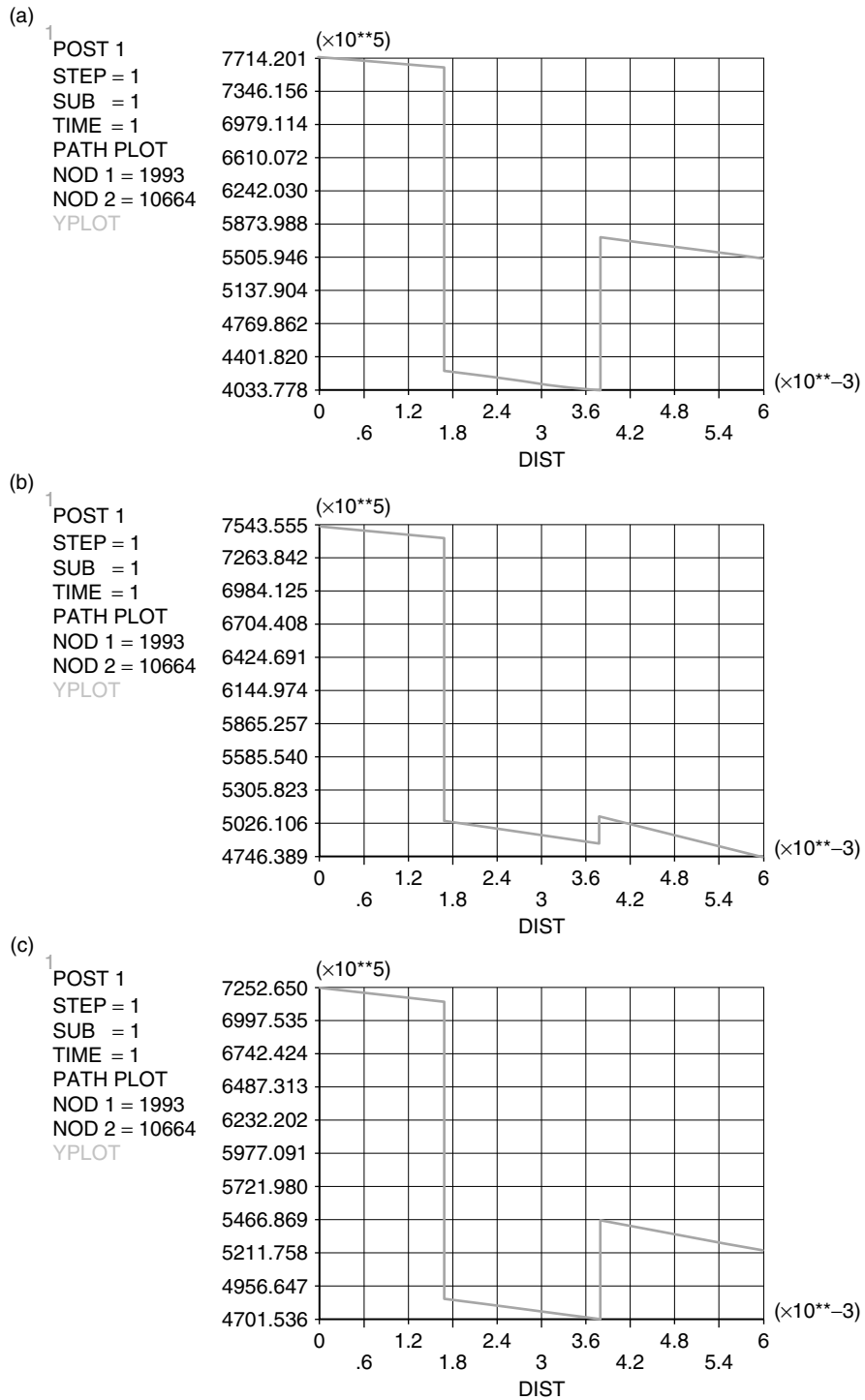
(a)

1
POST 1
STEP = 1
SUB = 1
TIME = 1
PATH PLOT
NOD 1 = 1993
NOD 2 = 10664
YPLOT

(×10**5)

7714.201
7346.156
6979.114
6610.072
6242.030
5873.988
5505.946
5137.904
4769.862
4401.820
4033.778

(×10**−3)

0   1.2   2.4   3.6   4.8   6
   .6   1.8   3   4.2   5.4

DIST

(b)

1
POST 1
STEP = 1
SUB = 1
TIME = 1
PATH PLOT
NOD 1 = 1993
NOD 2 = 10664
YPLOT

(×10**5)

7543.555
7263.842
6984.125
6704.408
6424.691
6144.974
5865.257
5585.540
5305.823
5026.106
4746.389

(×10**−3)

0   1.2   2.4   3.6   4.8   6
   .6   1.8   3   4.2   5.4

DIST

(c)

1
POST 1
STEP = 1
SUB = 1
TIME = 1
PATH PLOT
NOD 1 = 1993
NOD 2 = 10664
YPLOT

(×10**5)

7252.650
6997.535
6742.424
6487.313
6232.202
5977.091
5721.980
5466.869
5211.758
4956.647
4701.536

(×10**−3)

0   1.2   2.4   3.6   4.8   6
   .6   1.8   3   4.2   5.4

DIST

Figure 5.10   Distribution of the longitudinal (hoop) stress sq; at z = 0.4 h for the stacking sequence of (a) -45°/0°/-45°; (b) 45°/-45°/0° and (c) -45°/45°/-45°.

(a)
¹
POST 1
STEP = 1
SUB = 1
TIME = 1
PATH PLOT
NOD 1 = 1993
NOD 2 = 10664
XZPLOT

(×10**2)

1994.084
1569.609
1145.133
720.657
296.181
−128.294
−552.770
−977.246
−1401.722
−1826.198
−2250.674

(×10**−3)

0   1.2   2.4   3.6   4.8   6
   .6   1.8   3   4.2   5.4
              DIST

(b)
¹
POST 1
STEP = 1
SUB = 1
TIME = 1
PATH PLOT
NOD 1 = 1993
NOD 2 = 10664
XZPLOT

(×10**2)

512.460
321.146
129.827
-61.491
−252.810
−444.129
−635.448
−826.767
−1018.086
−1209.405
−1400.724

(×10**−3)

0   1.2   2.4   3.6   4.8   6
   .6   1.8   3   4.2   5.4
              DIST

(c)
¹
POST 1
STEP = 1
SUB = 1
TIME = 1
PATH PLOT
NOD 1 = 1993
NOD 2 = 10664
XZPLOT

(×10**2)

451.471
275.496
99.522
−76.451
−252.425
−428.399
−604.373
−780.347
−956.321
−1132.295
−1308.269

(×10**−3)

0   1.2   2.4   3.6   4.8   6
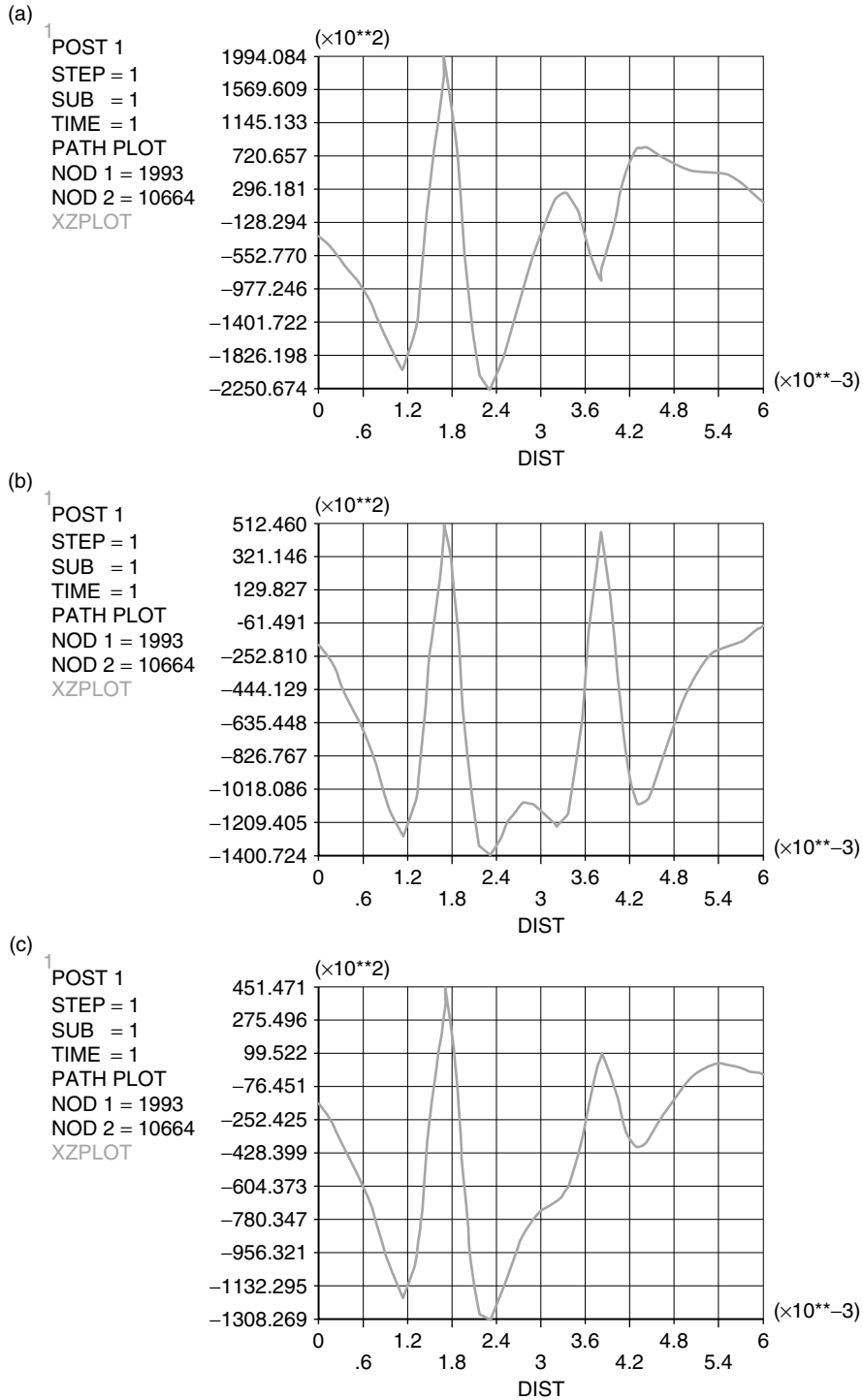   .6   1.8   3   4.2   5.4
              DIST

Figure 5.11   Distribution of the interlaminar shear stresses σ_{xz} at z = 0.4 h for the stacking sequence of (a) -45°/0°/-45°; (b) 45°/-45°/0° and (c) -45°/45°/-45°.

(a)

(b)

(c)
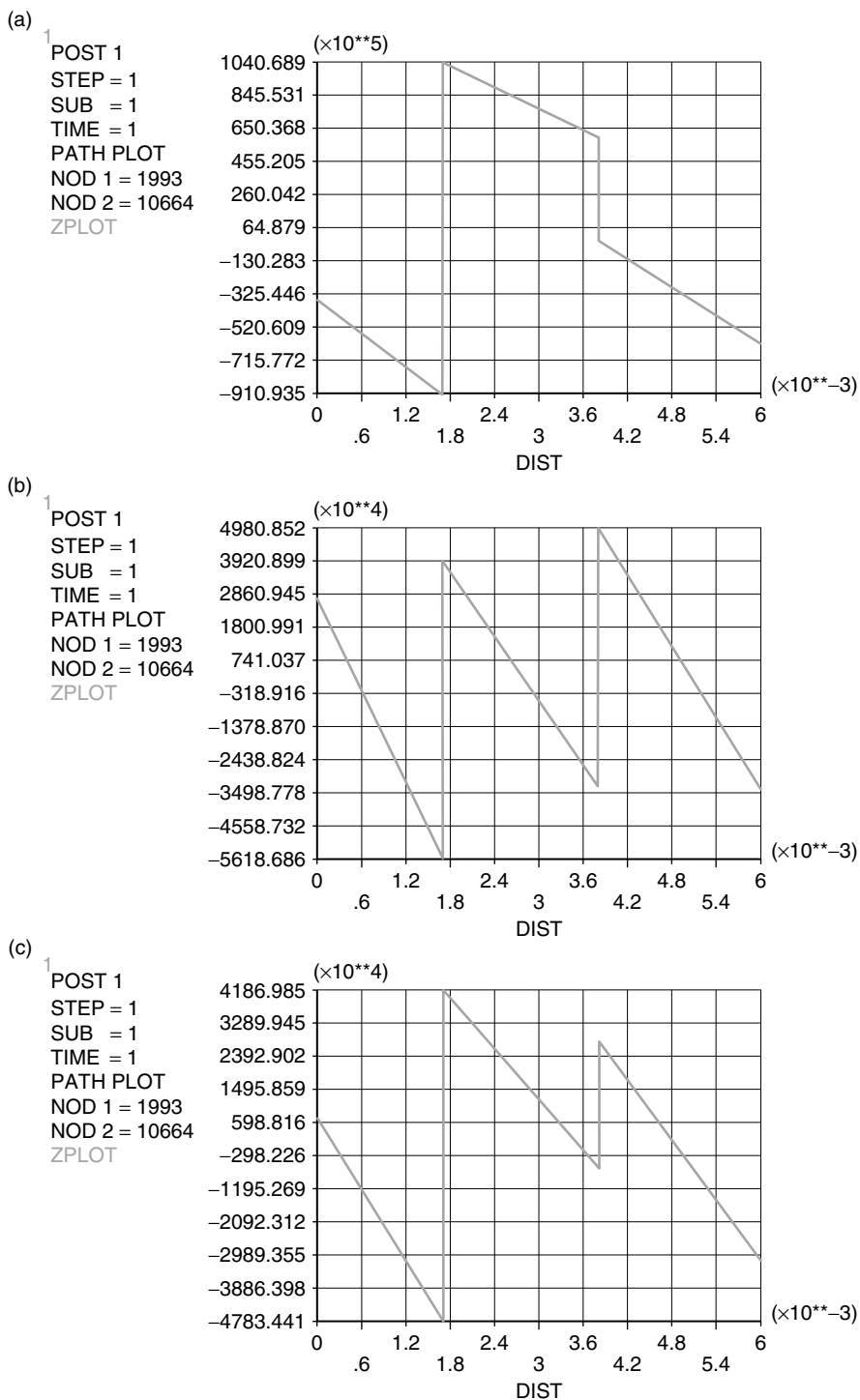

Figure 5.12   Distribution of the interlaminar normal stresses σ_z at z = 0.4 h for the stacking sequence of (a) -45°/0°/-45°; (b) 45°/-45°/0° and (c) -45°/45°/-45°.

4. CONCLUSION

The exponential cohesive zone modeling is used to simulate the stress distribution at the interface of material discontinuities in the rotating composite rotor. The single layer rotor was validated and the validation of the double layer finite element model was performed prior to incorporating the cohesive zone model to the rotating composite rotor. For the double layer model, it was discovered that the maximum longitudinal tensile stress at the outer layer (610 MPa) is higher than that of the inner layer (470 MPa). As the longitudinal tensile strength is more critical at the outer layer, triple layer rotor analyses are carried out in order to achieve a better performance in the outer layer. (Varatharajoo, R., Salit, M.S., and Goh, K.H., 2010).The results obtained from these models indicate the existence of severe out- of-plane stresses notably at the interfaces where the sudden material transitions occurred. The initiation of these stresses have been attributed to the onset of delamination and transverse cracking unique to hoop wound composite rotors, which if are to propagate to a substantial region of the rotor might result in the subsequent loss of strength and stiffness that would adversely affects the smooth operation of the flywheel. Here, varying the fiber stacking orientation to determine the most appropriate fiber recipe looks promising in mitigating these stresses. Of the few typical fiber orientations simulated, the 45¡/-45¡/0¡ fiber direction combination presents the best triple layer rotor among the few combination selected for analyses. Thus, the optimization of fiber orientation in the investigation of these stresses is especially crucial as well in the design of such high speed rotating structures.

APPENDIX A

THEORETICAL FORMULATION (TAHANI, NOSIER AND ZEBARJAD, 2005)

3.1. PLATE EQUATIONS OF MOTION

layerwise laminated plate theory for the displacement field:

$$u_1\left(x, y, z\right) = U_k\left(x, y\right)\Phi_k\left(z\right),$$
$$u_2\left(x, y, z\right) = V_k\left(x, y\right)\Phi_k\left(z\right),$$
$$u_3\left(x, y, z\right) = w_k\left(x, y\right)\Phi_k\left(z\right),$$

K = 1, 2, , N + 1,

local Lagrangian linear interpolation functions:

$$\Phi_k^1 = \frac{z_{k+1} - z}{h_k}, \Phi_k^2 = \frac{z - z_k}{h_k},$$

the global interpolation functions $\Phi_k(z)$:

$$\Phi_k\left(z\right) = \begin{cases} 0, z \leq z_{k-1}, \\ \Phi_{k-1}^2, z_{k-1} \leq z \leq z_k, \\ \Phi_k^1\left(z\right), z_k \leq z \leq z_{k+1}, \\ 0, z \geq z_{k+1}. \end{cases} \qquad k = 1, 2, ..., N + 1$$

Substituting into the linear strain-displacement equations for elasticity results in:

$$\varepsilon_r = \frac{\partial U_k}{\partial x}\Phi_k, \quad \varepsilon_\theta = \frac{1}{r}U_k\Phi_k, \quad \varepsilon_z = W_k\frac{\partial \Phi_k}{\partial_r},$$

$$\varepsilon_r\theta = \varepsilon_{\theta z} = 0, \qquad \varepsilon_{rz} = \frac{1}{2}\left(U_k\frac{d\Phi_k}{d_z} + \frac{\partial W_k}{\partial_r}\Phi_k\right)$$

3.2. EQUATIONS OF MOTION
The Hamilton principle for an elastic body is (Fung, 1965):

$$\int_{t_2}^{t_2}\left(\delta U + \delta V - \delta T\right)dt = 0$$

$$\delta U = 2\pi\int_{Rl}^{R_{l+1}}\int_{-h/2}^{h/2}\left(\sigma_r\delta\varepsilon_r + \sigma_\theta\delta\varepsilon_\theta + \sigma_z\delta\varepsilon_z + 2\sigma_{rz}\delta\varepsilon_{rz}\right)rdzdr$$

$$= -2\pi\int_{Rl}^{R_{l+1}}\left\{\left[\left(rM_r^k\right)_r - M_\theta^k - rQ_r^k\right]\delta U_k + \left[\left(rR_r^k\right)_r - rN_z^k\right]\delta W_k\right\}dr$$

$$+ 2\pi\left[rM_r^k\delta U_k\right]_{r=R_i}^{r=R_{i+1}} + 2\pi\left[rR_r^k\delta W_k\right]_{r=R_i}^{r=R_{i+1}}$$

Where

$$\left(M_r^k, M_\theta^k, R_r^k\right) = \int_{-h/2}^{h/2}\left(\sigma_r, \sigma_\theta, \sigma_{rz}\right)\Phi_k dz$$

$$\left(N_z^k, Q_r^k\right) = \int_{-h/2}^{h/2}\left(\sigma_z, \sigma_{rz}\right)\frac{d\Phi_k}{dz}dz$$

$$\delta V = -\int_\Gamma\int_{-h/2}^{h/2}\left(\bar\sigma_r\delta u_r + \bar\sigma_{rz}, \delta u_z\right)dzds$$

$$\delta V = -2\pi\int_{-h/2}^{h/2}r\left(\bar\sigma_r\Phi_k\delta u_k + \bar\sigma_{rz}\Phi_k\delta W_k\right)\Big|_{r=R_i}^{r=R_{i+1}}dz = -2\pi\left[r\bar M_r^k\delta U_k\right]_{r=R_i}^{r=R_{i+1}}$$

$$- 2\pi\left[r\bar R_r^k\delta W_k\right]_{r=R_i}^{r=R_{i+1}}$$

M_r^k and R_r^k are obtained by substituting σ_r ($\equiv \bar\sigma_r$) and σ_{rz} ($\equiv \bar\sigma_{rz}$) respectively, into the definitions of stress resultants M_r^k and R_r^k

In obtaining δT, the following must be noted:

$$\vec r = \left(r + u_r\right)\vec e_r + \left(z + u_z\right)\vec e_z, \qquad \vec v = \dot u_r\vec e_r + \left(r + u_r\right)\omega\vec e_\theta + \dot u_z\vec e_z$$

variation of the total kinetic energy can be written as

$$\int_{t_2}^{t_2} \delta T dt = 2\pi \int_{t_1}^{t_2} \int_{R_l}^{R_{l+1}} \int_{-h/2}^{h/2} \rho_i \left(\upsilon_r \delta \upsilon_r + \upsilon_\theta \delta \upsilon_\theta + \upsilon_z \delta \upsilon_z \right) r dr dz dt$$

$$= 2\pi \int_{t_1}^{t_2} \int_{R_l}^{R_{l+1}} \left(\overline{I}^k r \omega^2 \delta U_k + \overline{I}^{kj} \omega^2 U_j \delta U_k \right) r dr dt$$

Where

$$\left(\overline{I}^k, \overline{I}^{kj} \right) = \int_{-h/2}^{h/2} \rho_i \left(\Phi_k, \Phi_k \Phi_j \right) dz$$

Using the Hamilton s principle, the equations of motion for the ith ring can be obtained

$$\delta U_k : \frac{\partial M_r^k}{\partial r} + \frac{M_r^k - M_\theta^k}{r} - Q_r^k = -\overline{I}^k r \omega^2 - \overline{I}^{kj} U_j \omega^2,$$

$$\delta W_k : \frac{\partial R_r^k}{\partial r} + \frac{1}{r} R_y^k - N_z^k = 0$$

For the present LWT, the primary variables are U_k, W_k; whereas the secondary variables: are rM_r^k, rR_r^k

The linear constitutive relations for the kth orthotropic lamina with respect to the disk coordinate axes are (Herakovich, 1998):

$$\begin{Bmatrix} \sigma_\theta \\ \sigma_r \\ \sigma_z \\ \sigma_{rz} \\ \sigma_{\theta z} \\ \sigma_{r\theta} \end{Bmatrix}^{(k)} = \begin{bmatrix} C_{11} & C_{12} & C_{13} & 0 & 0 & 0 \\ C_{12} & C_{22} & C_{23} & 0 & 0 & 0 \\ C_{13} & C_{32} & C_{33} & 0 & 0 & 0 \\ 0 & 0 & 0 & C_{44} & 0 & 0 \\ 0 & 0 & 0 & 0 & C_{55} & 0 \\ 0 & 0 & 0 & 0 & 0 & C_{66} \end{bmatrix}^{(k)} \begin{Bmatrix} \varepsilon_\theta \\ \varepsilon_r \\ \varepsilon_z \\ 2\varepsilon_{rz} \\ 2\varepsilon_{\theta z} \\ 2\varepsilon_{r\theta} \end{Bmatrix}^{(k)}$$

the stress resultants are obtained as follows:

$$\left(N_z^k, M_r^k, M_\theta^k \right) = \left(B_{13}^{jk}, D_{11}^{kj}, D_{12}^{kj} \right) U_{j,r} + \frac{1}{r} \left(B_{23}^{jk}, D_{12}^{kj}, D_{22}^{kj} \right) U_j + \left(A_{33}^{jk}, B_{13}^{kj}, B_{23}^{kj} \right) W_j$$

$$\times \left(Q_r^k, R_r^k \right) = \left(A_{55}^{kj}, B_{55}^{kj} \right) U_j + \left(B_{55}^{jk}, D_{55}^{kj} \right) W_{j,r}$$

Where the rigidity terms are given by

$$\left(A_{pq}^{kj}, B_{pq}^{kj}, D_{pq}^{kj} \right) = \sum_{i=1}^{N} \int_{z_i}^{z_{i+1}} C_{pq}^{(i)} \left(\frac{d\Phi_k}{dz} \frac{d\Phi_j}{dz}, \Phi_k \frac{d\Phi_j}{dz}, \Phi_k \Phi_j \right) dz$$

2 (N + 1) equations of motion corresponding to 2 (N + 1) unknowns U_j and W_j:

$$D_{11}^{kj} \frac{d^2 U_j}{dr^2} + \frac{1}{r} D_{11}^{kj} \frac{dU_j}{dr} - \left(\frac{1}{r^2} D_{22}^{kj} + A_{55}^{kj} \right) U_j + \left(B_{13}^{kj} - B_{55}^{jk} \right) \frac{dW_j}{dr}$$

$$+ \frac{1}{r} \left(B_{13}^{kj} - B_{23}^{kj} \right) W_j = - \left(\bar{I}^k r + \bar{I}^{kj} U_j \right) \omega^2$$

$$\left(B_{55}^{kj} - B_{13}^{jk} \right) \frac{dU_j}{dr} + \frac{1}{r} \left(B_{55}^{kj} - B_{23}^{jk} \right) U_j + D_{55}^{kj} \frac{d^2 W_j}{dr^2} + \frac{1}{r} D_{55}^{kj} \frac{dW_j}{dr} - A_{33}^{kj} W_j = 0$$

REFERENCES

Baker, A.A. and Jones, R. (1988). Bonded Repair of Aircraft Structures. Dordrecht: Martinus Nijhoff Publishers.

Chue, C.H. and Liu, T.J.C. (1995). The Effects of Laminated Composite Patch with Different Stacking Sequences on Bonded Repair. Composite Engineering. 5:223–30.

Edward, K.T., Wilson, R.S. and McLean, S.K. (1989) Flexure of Simply Curved Composite Shapes, Composites 20,527–536 cited in Bhaskar, K. & Varadan, T. K. (1993)

Ibrahim M. M., Varatharajoo, R., Harun, H., Filipski Abdullah, N. (2005). Architecture for Combined Energy and Attitude Control System, American Journal of Applied Sciences- Sci. Publications, Vol. **2**, pp. 430–435.

Kirk, J. A., Schmidt, J. R., Sullivan, G. E., & Hromada, L. P. (1997). An Open Core Rotor Design Methodology, Aerospace and Electronics Conference, NAECON, Dayton, USA. pp. 594–600, 1997.

Pagano, N.J. and Pipes, R. B. (1973). Some Observations of the Interlaminar Strength of Composite Laminates, International Journal of Mechanical Science, Pergamon Press. 1973. Vol. 15, pp. 679–688.

Roithmayr, C. M., Karlgaard, C.D., Kumar, R.R., Bose, D.M. (2003). Integrated power and attitude control for a spacecraft with flywheels and control moment gyroscopes, in: Proceedings of 13th AAS/AIAA Space Flight Mechanics Meeting, No. AAS 03-124. American Astronautical Society, Springfield, VA, USA, pp. 1–20.

Tsiotras, P., Shen, H., Hall, C. (2001). Satellite attitude control and power tracking with energy/momentum wheels. Journal of Guidance, Control, and Dynamics 24 (1), 23–34.

Tahani, M., Nosier, A. & Zebarjad, S. M. (2005) Deformation and stress analysis of circumferentially fiber- reinforced composite disks. International Journal of Solids and Structures, Vol. 42, pp. 2741–2754.

Varatharajoo, R. (2006). Onboard Errors of the Combined Energy and Attitude Control System, Acta Astronautica – Pergamon/Elsevier, Vol. **58**, pp. 561–563.

Varatharajoo, R. (2006). Operation for the Combined Energy and Attitude Control System, J. Aircraft Engineering and Aerospace Technology- Emerald, Vol. **78**, pp. 495–501.

Varatharajoo, R. and Fasoulas S. (2002). Methodology for the Development of Combined Energy and Attitude Control Systems for Satellites, J. Aerospace Science & Technology - Elsevier, Vol. **6**, pp. 303–311.

Varatharajoo, R. and Fasoulas S. (2005). The Combined Energy and Attitude Control System for Small Satellites -Earth Observation Missions, Acta Astronautica – Pergamon/Elsevier, Vol. **56**, pp. 251–259.

Varatharajoo, R. and Kahle, R. (2005) A Review of Conventional and Synergistic Systems for Small Satellites. Aircraft Engineering and Aerospace Technology. Vol. 77 (2005). pp. 131–141, 2005.

Varatharajoo, R. and Kahle R. (2005). A Review of Spacecraft Conventional and Synergistic Systems, Vol. **77**, pp. 131–141, J. Aircraft Engineering and Aerospace Technology- Emerald.

Varatharajoo, R. (2004). A Combined Energy and Attitude Control System for Small Satellites, Acta Astronautica – Pergamon/Elsevier, Vol. **54**, pp. 701–712, 2004.

Varatharajoo, R. and Filipski Abdullah, F. (2004). Attitude Performance of the Spacecraft Combined Energy and Attitude Control System, J. British Interplanetary Society - BIS, Vol. **57**, pp. 237–241.

Varatharajoo, R., Salit, S.S., Goh, K.H. (2010). Material Optimization of Carbon/ Epoxy Composite Rotor for Spacecraft Energy Storage. International Journal of Multiphysics. Vol. 4 (2) 2010.

Varatharajoo, R. and Tarmizi M. A. (2004). Flywheel Energy Storage for Spacecraft, J. Aircraft Engineering and Aerospace Engineering Technology- Emerald, Vol. **76**, pp. 384–390.

Varatharajoo, R., Wooi C. T., Mailah M. (2011). Two Degree-of-freedom Spacecraft Attitude Controller, Advances In Space Research, Vol. **47** (4), pp. 685–689.

Wilkins, D.J. (1983). A preliminary damage tolerance methodology for composite structures. Failure Analysis and Mechanisms of Failure of Fibrous Composite Structures. NASA CP–2278.

Xu, X.P., Needleman, A. (1994). Numerical simulations of fast crack growth in brittlesolids. Journal Mechanics and Physics of Solids, Vol. 42 (9), pp. 1397–1434.